water

MDPI

Article

Short-Term Sediment Dispersal on a Large Retreating Coastal River Delta via ^{234}Th and ^{7}Be Sediment Geochronology: The Mississippi River Delta Front

Andrew Courtois [1,*], Samuel Bentley [2], Jillian Maloney [3], Kehui Xu [4], Jason Chaytor [5], Ioannis Y. Georgiou [1], Michael D. Miner [1], Jeffrey Obelcz [6], Navid H. Jafari [7] and Melanie Damour [8]

1 The Water Institute, New Orleans, LA 70122, USA; igeorgiou@thewaterinstitute.org (I.Y.G.); mminer@thewaterinstitute.org (M.D.M.)
2 Department of Geology and Geophysics, Coastal Studies Institute, Louisiana State University, Baton Rouge, LA 70803, USA; sjb@lsu.edu
3 Department of Earth and Environmental Sciences, San Diego State University, San Diego, CA 92182, USA; jmaloney@sdsu.edu
4 Department of Oceanography and Coastal Sciences, Coastal Studies Institute, Louisiana State University, Baton Rouge, LA 70803, USA; kxu@lsu.edu
5 United States Geological Survey, Woods Hole, MA 02543, USA; jchaytor@usgs.gov
6 Ocean Sciences Division, United States Naval Research Laboratory, Stennis Space Center, MS 39529, USA; jeffrey.obelcz@nrlssc.navy.mil
7 Department of Civil and Environmental Engineering, Coastal Studies Institute, Louisiana State University, Baton Rouge, LA 70803, USA; njafari@lsu.edu
8 Bureau of Ocean Energy Management, New Orleans, LA 70123, USA; melanie.damour@boem.gov
* Correspondence: acourtois@thewaterinstitute.org

Abstract: Many Mississippi River Delta studies have shown recent declines in fluvial sediment load from the river and associated land loss. In contrast, recent sedimentary processes on the subaqueous delta are less documented. To help address this knowledge gap, multicores were collected offshore from the three main river outlets at water depths of 25–280 m in June 2017 just after the peak river discharge period, with locations selected based on 2017 U.S. Geological Survey seabed mapping. The coring locations included the undisturbed upper foreset, mudflow lobes, gullies, and the undisturbed prodelta. Nine multicores were analyzed for Beryllium-7 activity, and four cores were analyzed for excess Thorium-234 activity via gamma spectrometry, granulometry and X-radiography. Our results indicate a general trend of declining ^{7}Be and ^{234}Th activities and inventories with increasing distance from sources and in deeper water. The core X-radiographs are graded from the predominantly physically stratified nearshore to the more bioturbated offshore, consistent with the sedimentation patterns. Sediment focusing assessed via the ^{7}Be and ^{234}Th sediment inventories shows preferential sedimentation in gully and lobe environments, whereas the upper foreset and prodelta focusing factors are relatively depleted. Overall, short-term sediment deposition from the main fluvial source remains active offshore from all three major river outlets, despite the overall declining river load.

Keywords: Mississippi River Delta Front; submarine landslide; sedimentation; radionuclide

Citation: Courtois, A.; Bentley, S.; Maloney, J.; Xu, K.; Chaytor, J.; Georgiou, I.Y.; Miner, M.D.; Obelcz, J.; Jafari, N.H.; Damour, M. Short-Term Sediment Dispersal on a Large Retreating Coastal River Delta via ^{234}Th and ^{7}Be Sediment Geochronology: The Mississippi River Delta Front. *Water* **2024**, *16*, 463. https://doi.org/10.3390/w16030463

Academic Editors: Yijun Xu and Heqin Cheng

Received: 18 December 2023
Revised: 16 January 2024
Accepted: 24 January 2024
Published: 31 January 2024

1. Introduction

River deltas are sedimentary gateways between terrestrial river catchments and continental shelf and deep-sea environments. Sediment dispersal through and within subaqueous portions of deltas occurs via hydrodynamic processes and mass wasting, which is globally important in river deltas [1–3], but less studied than hydrodynamic processes. Subaqueous deltaic morphology and stratigraphy are strongly influenced by the combined effects of sediment supply, waves, tides, and gravity-driven flow, and studies in the last two decades have determined that sediment transport aided by gravity-driven phenomena

is more widespread than previously understood [4–8]. The Mississippi River Delta Front (MRDF) is an area extending offshore of the Mississippi River Delta (MRD) at water depths of ~10–250 m with distinct morphological features related to gravity-driven sediment transport [2,9]. The MRD is economically valuable in terms of marine transportation, fisheries, and oil and gas production and transport [10]. Although an extensive body of literature documents subaqueous mass wasting on the MRDF [2,11–15], the last regional seabed survey completed on the MRDF occurred in the late 1970s [9]. Since that time, the MRD has begun to shift from net progradation to at least partial backstepping due to reductions in sediment supply and the landward re-routing of dispersal patterns [15,16]. Nevertheless, geohazards remain active [17], and many questions remain unanswered regarding triggers, sediment flux, and spatial and temporal scales of seabed failure [2]. This study's analysis of the MRDF's short-term sediment dispersal patterns is an initial step towards a larger-scale investigation [14,15,17–19], initiated by the Bureau of Ocean Energy Management in 2022 to address these questions using new technology and methods that have been developed since Coleman's (1981) work [9].

The largest mass wasting events on the MRDF are triggered primarily by hurricane waves and have caused major damage to oil and gas infrastructure, toppling platforms and disrupting pipelines [2,17,20]. The impacts of these events on offshore structures have been known since the 1970s [21]. The modern MRD region contains infrastructure responsible for nearly 20% of US hydrocarbon production [22], demonstrating the economic implications of these geohazards.

In addition to hurricane waves, rapid sedimentation along the MRDF is also a contributing factor to submarine landslides [23]. High sedimentation rates >1 m/yr have been measured adjacent to distributary mouths [9]. However, more recent changes in seabed morphology near river outlets show that portions of the MRDF are retreating landward rather than prograding [15]. Research suggests that sediment is initially deposited within ~30 km offshore of Southwest Pass and sediment focusing occurs proximal to Southwest Pass [24,25]. One study which focused on the Southwest Pass region indicates that the highest sediment deposition rates (SDRs) are observed proximal to the river outlet and SDRs do not correlate between depositional environments located similar distances from the river outlet [18]. To gain a broader regional perspective coupling present-day MRDF seabed morphology and sedimentation patterns and to test geological and geophysical tools for effectiveness in this environment, new preliminary regional geophysical and coring surveys were conducted in 2017. These surveys were geographically focused on regions offshore of major river outlets, encompassing <15% of the MRDF area. The main objective of our research is to evaluate the sedimentation rates and dispersal patterns of Mississippi River (MR) sediment using short-lived radiochemical tracers (^{7}Be and ^{234}Th) and similar methods to those of Corbett et al. (2004) [24], Corbett et al. (2007) [25] and Keller et al. (2017) [18], but encompassing a larger geographic region and with the cores targeted using new geophysical data [26] postdating Corbett et al. (2007) [25] and Keller et al. (2017) [18]. Expanding on Keller et al. (2017) [18], we hypothesize that initial sediment deposition may be controlled by initial plume dynamics (as observed by Keller et al., 2017) [18], but that subsequent remobilization and deposition via mass transport phenomena creates multi-stage dispersal [8,27,28] due to both gravity-driven flow and reduced bed shear stress from waves in deeper water which may produce sediment focusing within specific depositional settings, such as gullies and lobes (Figures 1–3). Such patterns can be elucidated via sediment radioisotope geochronology, supported by an analysis of the sedimentary fabric to assess bioturbation (under a relatively slow sedimentation rate) and physical stratification (under a relatively faster sedimentation rate) [29]. It is important to note that this study focuses on sedimentary processes observed within relatively short timeframes (less than ~eight months) and offers insights into mass wasting events occurring over longer temporal scales (annual to decadal).

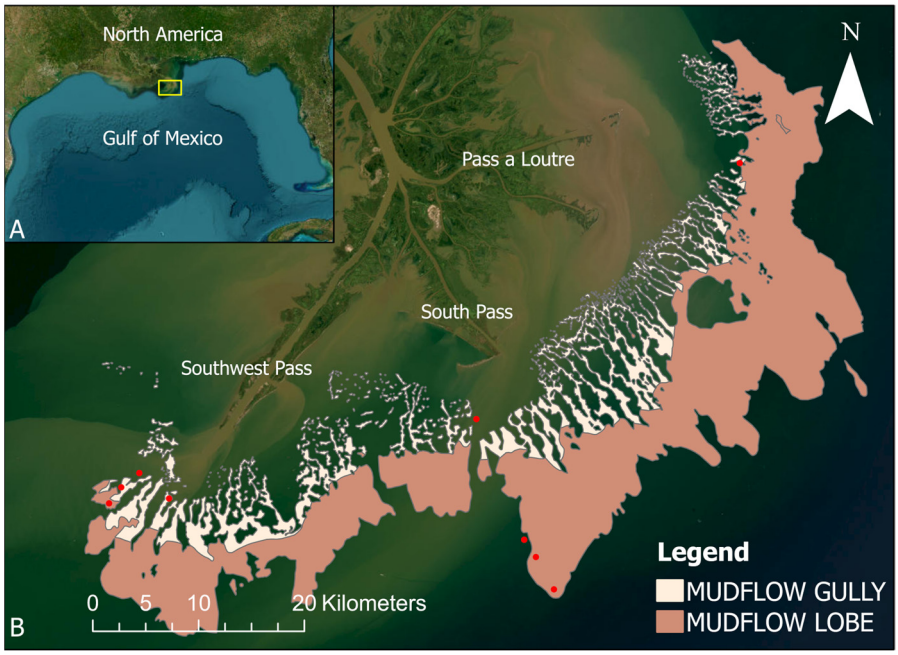

Figure 1. Overview of study area location (**A**) and regional extent of mudflow gullies and lobes on the Mississippi River Delta Front [30] with coring locations denoted by red circles (**B**). Base map provided by Earthstar Geographics via Esri.

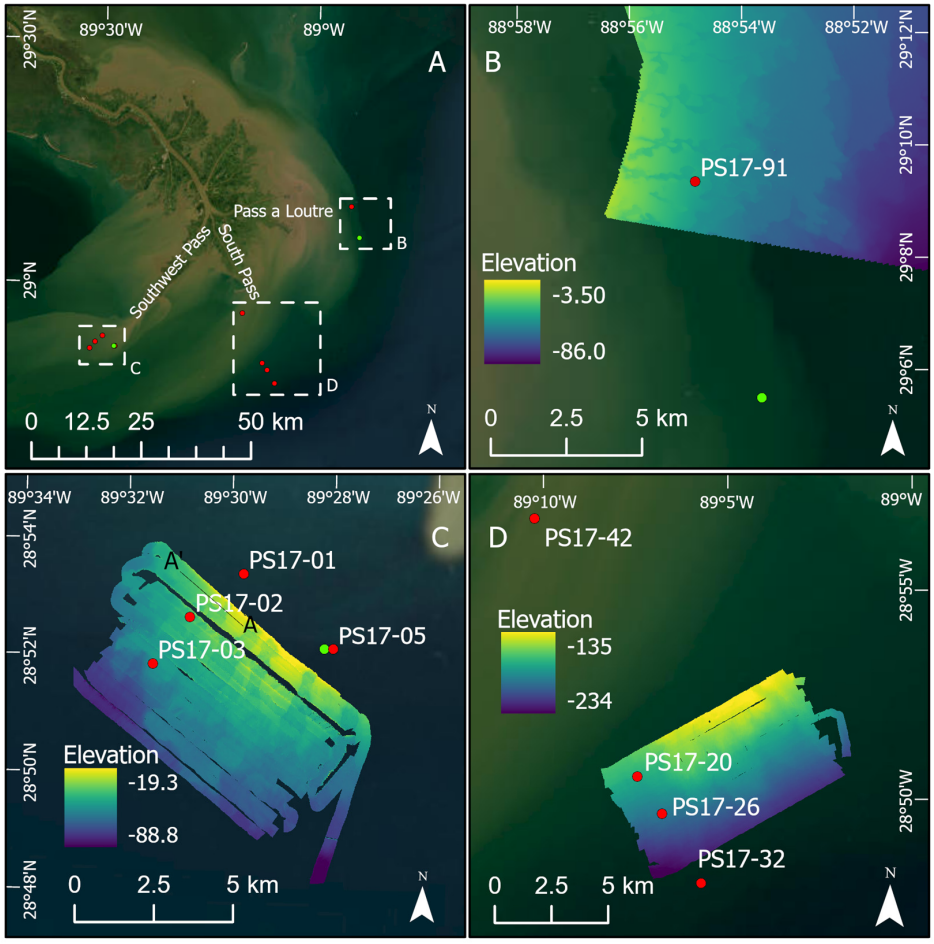

Figure 2. Map of study area showing Mississippi River Delta Front (**A**), Pass a Loutre (**B**), Southwest Pass (**C**) and South Pass (**D**). Core locations are denoted by red circles. CTD cast locations are denoted

by green circles. Seismic line is denoted by black line in Southwest Pass labeled A–A′ (**C**). Panel A shows approximate locations (white squares) for bathymetry data shown in panels (**B**–**D**). Bathymetric data [26] are shown with elevation reported in meters (NAVD 88). Bathymetry data shown in panels (**B**–**D**) have different scales due to being separate datasets. Base map provided by Earthstar Geographics via Esri.

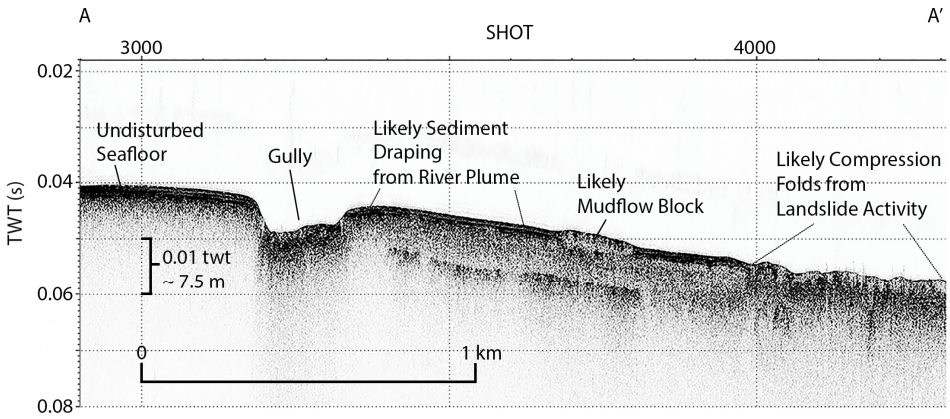

Figure 3. Sub-bottom seismic data [26] depicting various seabed features commonly found along the Mississippi River Delta Front. Data collected near Southwest Pass; see black line A–A′ in Figure 2C for location.

2. Methodology

2.1. Study Site

The study area encompasses the MRDF along the Louisiana continental shelf offshore of the MR's lowermost major distributaries: namely, Southwest Pass (SW Pass), South Pass (S Pass) and Pass a Loutre (PAL) (Figure 1). Core sites are located <25 km from the mouth of the MR at water depths ranging between 27 m and 258 m (Figure 2).

The MR is the largest riverine system in North America and possesses a drainage basin of 3.4×10^6 km^2; the MRD is classified as a fluvially dominated delta [5,31]. The MR has experienced a declining sediment load over the past ~100 yr due to multiple anthropogenic factors [16,32,33] and has an estimated annual sediment load of 157 Mt/yr (million metric tons per year) near Baton Rouge, Louisiana, calculated during 2008–2010 [34], with fine silt and clay comprising ~80% of the total suspended load [35]. Suspended sediment loads leaving SW Pass, S Pass, and PAL were estimated as 20.8, 4.7 and 4.8 Mt/yr during 2008–2010, respectively [34]. Since then, S Pass and PAL discharges may have been partially blocked due to in-channel dredge spoil disposal and associated in-channel sedimentation [36], with smaller fractions of total upstream load likely now exiting these major river outlets [37].

Coleman et al. (1998) [38] subdivided the subaqueous delta front into four areas according to depth: interdistributary bays (0–10 m), upper delta front (10–70 m), intermediate delta front (70–120 m) and lower delta front (120–200 m), bordered in the seaward direction by prodelta (extending out to ~300 m), with each having common morphological features unique to their location. The delta front corresponds broadly to the foresets of a deltaic clinothem, and the prodelta corresponds to a deltaic clinothem bottomset [39]. The most distinctive morphological features of the MRDF are mudflow gullies and mudflow lobes. Gullies are typically tens of kilometers in length and hundreds of meters in width, occurring in water depths of approximately 5–90 m with steep gradients flanking the edges up to 19° [13] (Figure 1). Mudflow gullies incise clinothem foresets and merge downslope into mudflow lobes with positive relief. Lobes are depocenters for sediment transported downslope from gullies and can often stack on one another and intersect through time. Lobes vary in thickness but are generally <10 m thick. Mudflow gullies and lobes on the MRDF are commonly found on slopes ranging between 0.5° and 1.5° [13], but slope failures have occurred in areas with a slope <0.3° [21].

2.2. Evidence of Mass Failures and Triggering Mechanisms

Mudflow gullies and lobes are produced from an interaction of high sediment input via the MR and slope failure, occurring on variable seabed slopes [13,21]. Maloney et al. (2018) [15] highlighted mudflow lobe accretion and advancement in regions off SW Pass and S Pass with areas off PAL remaining quiescent (using similar approaches with more advanced technology and more recent data than those of Coleman et al., 1980) [13].

Previously, most research related to seabed failures along the MRDF was conducted in response to major infrastructure damage and mudflows initiated by hurricane waves [15,23,40]. However, Obelcz et al. (2017) [14] documented seabed movement during relatively quiescent periods, suggesting that annual winter storm waves may also trigger flows. Similarly, Maloney et al. (2018) [15] documented recent mudflow morphodynamics despite reduced sedimentation rates, highlighting the need for more research on triggering mechanisms of failure events and long-term implications of reduced sediment discharges. Additionally, repeat bathymetric surveys have tracked the movement of individual mud flow debris blocks during periods without major hurricanes [17].

2.3. Fieldwork and Core Sampling/Processing

Field work was performed in early June 2017 aboard the *R/V Point Sur* offshore of the MR's main distributary outlets (SW Pass, S Pass and PAL). Seafloor morphologies sampled included undisturbed upper foresets (uuf), mudflow gullies (gul), mudflow lobes (lob) and prodelta (pro). Sampling locations were determined using multi-beam bathymetry and sub-bottom seismic data (Figures 2 and 3) collected by the United States Geological Survey (USGS) in May 2017 [26]. Cores were collected approximately ten days after peak river discharge in late May 2017, using an Ocean Instruments MC-800 multicore (Ocean Instruments, Fall City, WA, USA) with eight sampling tubes 10 cm diameter and 70 cm long and with nominal recovery of cores that were 50 cm long.

Following initial collection, a single core was chosen for radiochemical and grain-size analyses, a second core for X-radiography and a third core to be archived for future studies. Cores used for radiochemical and grain-size analyses were extruded on deck and subsampled at 2 cm intervals. Core slabs for X-radiography (2 cm thick) were subsampled by inserting an open three-sided Plexiglass tray into the core tube then sealed by inserting a fourth side to prevent distortion of the sedimentary fabric. Additional radionuclide, grain-size, and X-radiography data can be found in Supplementary Materials [41].

2.3.1. Radionuclide Analysis

Radionuclides of interest for this study include ^{7}Be (natural cosmogenic, $t_{1/2}$ = 53.2 days, 477 keV peak) and ^{234}Th (natural ^{238}U series, $t_{1/2}$ = 24.1 days, 63 keV peak), both of which can be used as tracers of short-term sediment deposition due to their particle reactivity and short half-life. Cosmogenic ^{7}Be is produced naturally in the atmosphere, then deposited from dry deposition and/or precipitation and adsorbed onto sediments [42]. It is often used as a tracer for fluvially sourced sediments to measure short-term sediment accumulation rates due to its relatively short half-life and tendency to become concentrated in fluvial sediments above background activities in open-marine settings [18,24,25,43]. ^{234}Th is continuously produced in marine waters from the decay of its parent, ^{238}U. Due to its short half-life and the predominance of ^{234}Th production in marine waters, this study uses ^{234}Th as a proxy for short-term sediment deposition rates and an indicator of marine resuspension events.

Samples were weighed and dried for 24 h to determine water content, then powdered using a mortar and pestle and sealed into petri dishes (10–15 g of dry sediment per sample). Two Canberra low-energy germanium detectors (Canberra/Mirion Technologies, Meriden, CT, USA; calibrated using IAEA reference materials RGU-1 and IAEA 135) were used for radionuclide measurement, with individual cores being restricted to one detector. Samples analyzed for ^{7}Be and ^{234}Th were counted for 24 h within one half-life (for the radioisotope of interest) from the date of collection. Self-absorption of ^{234}Th gamma photons was estimated using the transmission method [44]. Samples were initially analyzed

for ^{234}Th and recounted after 6 months to quantify excess ^{234}Th, (total ^{234}Th activity—supported ^{234}Th activity). Data are reported in decays per minute per gram (dpm/g), with 1 dpm/g = 60 Bq/g. Sediment deposition rates (SDRs; cm/day) were calculated for both ^{7}Be and ^{234}Th via regressions of data using Equation (1) [45]:

$$A_z = A_0 e^{(-\lambda z/SDR)} \quad (1)$$

where A_z is activity (dpm/g) at depth z (cm), A_0 is activity extrapolated to the surface (dpm/g), λ is the decay constant of ^{7}Be (0.01305 day^{-1}) or ^{234}Th (0.02876 day^{-1}) and SDR is the sediment deposition rate (cm/day).

Local focusing of sediment deposition can be assessed by comparing inventories of ^{7}Be and ^{234}Th with equilibrium inventories expected from vertical flux to the seabed in the absence of lateral advection. Sediment inventories of ^{7}Be and $^{234}Th_{xs}$ in cores were calculated using Equation (2) [45]:

$$I = \Sigma \rho_s \Delta z (1 - \Phi_i) A_i \quad (2)$$

where I is inventory (disintegrations per minute/centimeter^2, dpm/cm^2), ρ_s is grain density (g/cm^3), assumed to be 2.65 g/cm^3, Δz is the thickness of sample (2 cm), Φ_i is porosity calculated by water loss at 60 °C for 24 h and A_i is activity (dpm/g).

Two regional Gulf of Mexico studies of vertical ^{7}Be flux and inventories were averaged to calculate a reference ^{7}Be inventory of 10.1 dpm/cm^2: that of Baskaran et al., 1993 [46] (14.7 dpm/cm^2) and that of Corbett et al., 2004 [24] (5.4 dpm/cm^2).

Equilibrium inventories of ^{234}Th were estimated using the approach of Adhikari et al. (2016) [47]. The parent isotope ^{238}U concentrations were first estimated as a function of water column salinity using Equation (3) [48]:

$$^{238}U(\pm 0.047) = 0.0786 \times S - 0.315 \quad (3)$$

where ^{238}U is measured in (dpm/cm^3) and S is salinity (SI units). Two locations (proximal to SW Pass sites; proximal to PAL site) were used for salinity data that were supplied from underway conductivity, temperature and depth (CTD) casts in May 2017 in the study area [26]. Then, ^{234}Th flux (F, dpm/cm^{-2} d^{-1})) was calculated using Equation (4) [47]:

$$(F_{Th})_z = \lambda_{Th} \int (A_{238U} - A_{234Th}) dz \quad (4)$$

where A is water column activities of ^{238}U or ^{234}Th (dpm/cm^3), λ_{Th} is the radioactive decay constant for ^{234}Th and $(F_{Th})_z$ is the integrated water column flux (dpm/cm^2 per day) of ^{234}Th at depth 'z' (m). This model assumes that ^{234}Th produced from ^{238}U decay is rapidly scavenged and transported to the seabed. The equilibrium background ^{234}Th inventory (I, dpm/cm^2) was calculated using Equation (5) [45]:

$$F = \lambda I \quad (5)$$

where F is ^{234}Th flux in the water column, and λ is the ^{234}Th decay constant (0.02876 day^{-1}). Focusing factors were estimated using Equation (6) [45]:

$$FF = I_c / I_b \quad (6)$$

where FF is focusing factor, I_c is core inventory (dpm/cm^2) and I_b is estimated equilibrium inventory (dpm/cm^2). Uncertainty in core inventories is represented as average analytical uncertainties in activity measurements for each core.

2.3.2. Grain Size Analysis

Wet sediment samples (<1 mL) were placed in test tubes with 40 mL of a 0.05% sodium hexametaphosphate solution (Thermo Fisher Scientific, Waltham, MA, USA) and immersed

in an ultrasonic bath to facilitate disaggregation. Several samples were tested with and without removal of organics via H_2O_2 oxidation; negligible differences were observed between treatments, so no H_2O_2 treatment was applied to remaining samples [18]. Samples were measured in a Beckham Coulter laser diffraction particle analyzer (Model LS 13 320; Beckham Coulter, Inc., Indianapolis, IN, USA). Volume–frequency contour plots were generated for all cores using SigmaPlot© (Version 14.5). A total number of 242 samples, sampled at 2 cm intervals, were analyzed for this study.

2.3.3. X-Radiography

X-radiography was performed using a portable MinXray HF8015+dlp X-ray generator (Médical Tronik, Laval, QC, CA) illuminating a Samsung Model SP501 X-ray digital detector panel (North Star Imaging, Allen, TX, USA). Image brightness and contrast were adjusted using ImageJ© (Version 1.51) and Adobe Illustrator© (Version 21), and images are shown with annotations for specific sedimentary features. Measurements of bioturbation intensity down core were created through visual identification of physical versus biogenic features in X-radiographs on 1 cm grids, then averaged horizontally.

2.4. Bed Shear Stress Estimation

Wave data from the National Oceanic and Atmospheric Administration (NOAA) buoy 42040 (https://www.ndbc.noaa.gov/), accessed on 7 December 2022, were processed to estimate inshore bed shear stresses produced by waves alone. Bed shear stress calculations were made by using NOAA measurements of wave period, deep water wave height and inshore water depth, as well as by using equation 106 and related methods from Wright (1995) [49] to estimate wavelength and equations 62 and 57 from Soulsby (1997) [50] to estimate wave friction factor and wave skin friction shear stress (t_w), respectively.

3. Results

3.1. Radionuclide Analysis

Tables 1 and 2 contain descriptions of the core locations, the depositional environment derived from multibeam mapping (Figure 2) and a summary of the $^{234}Th_{xs}$ and ^{7}Be data. Four cores (PS17-02, PS17-03, PS17-05 and PS17-91) were analyzed for both ^{7}Be and $^{234}Th_{xs}$ (Figure 4) due to rapid ^{234}Th decay, and five additional cores analyzed for ^{7}Be only.

Table 1. Summary of cores analyzed for excess Thorium-234. Sediment deposition rate is shown as SDR. Theoretical Thorium-234 inventory is derived from Equations (3)–(5). Excess Thorium-234 core inventory is calculated from Equation (2). Excess Thorium-234 sediment deposition rate (SDR) is derived from Equation (1) and SDR R^2 reflects fit to Equation (1).

Core ID	Water Depth (m)	Distance from Pass (km)	Facies	^{234}Th Theoretical Inventory (dpm/cm^2)	$^{234}Thxs$ Core Inventory (dpm/cm^2)	$^{234}Thxs$ Penetration Depth (cm)	$^{234}Thxs$ SDR (cm/Day)	SDR R^2
PS17-02	51	11	gul	5.78	33.7	12 ± 1	0.11 ± 0.01	0.98
PS17-03	60	13	lob	5.78	24.1	14 ± 1	0.06 ± 0.01	0.97
PS17-05	27	8	gul	5.78	44.4	18 ± 1	N/A	N/A
PS17-91	40	14	gul	18.32	79.5	18 ± 1	0.28 ± 0.07	0.77

Table 2. Summary of cores analyzed for Beryllium-7.

Core ID	Water Depth (m)	Distance from Pass (km)	Facies	^{7}Be Theoretical Inventory (dpm/cm^2) [a]	^{7}Be Theoretical Inventory (dpm/cm^2) [b]	^{7}Be Core Inventory (dpm/cm^2)	^{7}Be Penetration Depth (cm)	^{7}Be Surface Activity (dpm/g)	^{7}Be SDR (cm/Day) [c]	SDR R^2
PS17-01	31	9	uuf	14.7	5.4	3.91	4 ± 1	4.35	0.016	1
PS17-02	51	11	gul	14.7	5.4	9.15	10 ± 1	5.17	0.05 ± 0.01	0.97
PS17-03	60	13	lob	14.7	5.4	6.62	6 ± 1	7.22	0.03 ± 0.01	0.97

Table 2. *Cont.*

Core ID	Water Depth (m)	Distance from Pass (km)	Facies	^{7}Be Theoretical Inventory (dpm/cm^2) [a]	^{7}Be Theoretical Inventory (dpm/cm^2) [b]	^{7}Be Core Inventory (dpm/cm^2)	^{7}Be Penetration Depth (cm)	^{7}Be Surface Activity (dpm/g)	^{7}Be SDR (cm/Day) [c]	SDR R^2
PS17-05	27	8	gul	14.7	5.4	37.6	26 ± 1	N/D	0.69 ± 0.79	0.08
PS17-20	187	18	uuf	14.7	5.4	0.66	2 ± 1	1.17	N/D	N/D
PS17-26	206	20	uuf	14.7	5.4	0.39	2 ± 1	0.98	N/D	N/D
PS17-32	258	23	pro	14.7	5.4	N/D	N/D	N/D	N/D	N/D
PS17-42	39	7	gul	14.7	5.4	13.2	22 ± 1	4.98	0.06 ± 0.01	0.9
PS17-91	40	14	gul	14.7	5.4	18.5	16 ± 1	4.82	0.12 ± 0.03	0.81

Beryllium-7 theoretical inventory [a] was sourced from Baskaran et al. (1993) [46] and Beryllium-7 theoretical inventory [b] was sourced from Corbett et al. (2004) [24]. Beryllium-7 core inventory was calculated using Equation (2). Beryllium-7 sediment deposition rate (SDR) [c] was derived from Equation (1) and SDR R^2 reflects fit to Equation (1). N/D denotes not detectable.

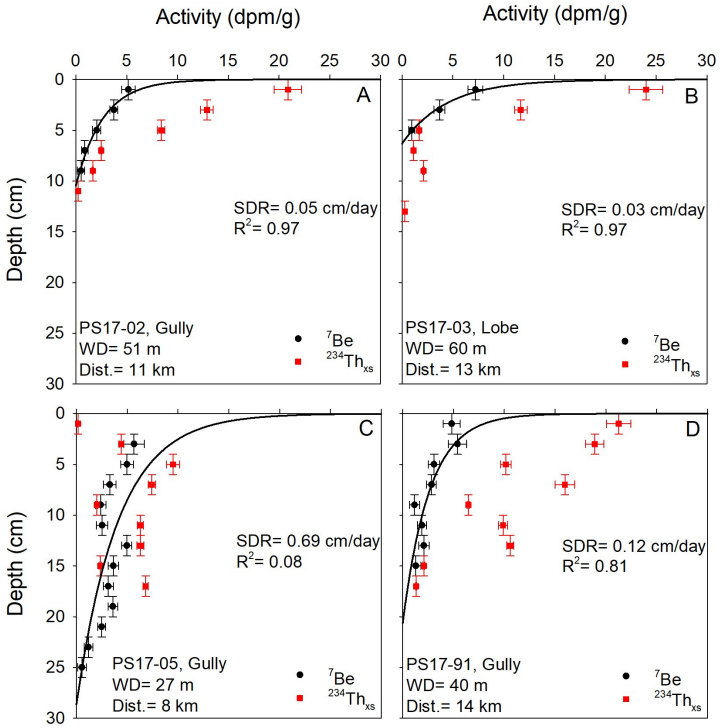

Figure 4. Beryllium-7 (black circles) and excess Thorium-234 (red squares) activities from cores located in Southwest Pass (**A**–**C**) and Pass a Loutre (**D**). Cores sampled include both gully (**A**,**C**,**D**) and mudflow lobe (**B**) morphology. Water depth (WD) and distance from closest outlet (Dist.) are denoted. Sediment deposition rate (SDR) is derived from Equation (1), and R^2 values shown are calculated from Beryllium-7 activity. Black lines reflect fit of Equation (1) to Beryllium-7 activity.

The core locations within 15 km of the MR and at water depths less than 60 m on average exhibit ^{7}Be surface activities of ~5 dpm/g, except for SW Pass site PS17-05 (Table 2). South Pass sites PS17-20 and PS17-26 exhibit ^{7}Be surface activities of ~1 dpm/g and are located in deeper water (>185 m) and farther from the MR (>18 km) (Table 2). The cores analyzed for $^{234}Th_{xs}$ are all located within 15 km of the MR and lie in waters shallower than 60 m (Table 1). ^{7}Be was detected in eight out of the nine core locations. ^{7}Be was not detected at site PS17-32, which is the most distal core location in the study area, located approximately 23 km from S Pass at a 258 m water depth. The mudflow gully core locations off of all the MR's main distributaries (SW Pass, S Pass and PAL) exhibited the largest inventories, penetration depth and SDRs with regard to ^{7}Be. These locations are less than 15 km from the nearest dominant river outlet and at water depths less than ~50 m.

The core inventories of both ^{7}Be and ^{234}Th$_{xs}$ tend to be highest in the gully depositional environments, followed by the lobes and then the undisturbed upper foreset (Tables 1 and 2). Focusing factors (Equation (6)) for the ^{234}Th$_{xs}$ and ^{7}Be inventories are shown in Figure 5A,B. For ^{234}Th$_{xs}$, FF > 1 for all four of the cores (three gully cores and one lobe core). For the ^{7}Be inventories (Table 2, Figure 5A) in the three gully cores, FF $\geq$ 1 (within uncertainty derived from activity measurements). The ^{7}Be inventories (Table 2, Figure 5A) for the undisturbed upper foreset and lobe cores yield FF < 1 (Figure 5B). Overall, the focusing factors for both ^{7}Be and ^{234}Th$_{xs}$ tend to be elevated in the gully locations (Figure 5A) and tend to decline with increasing distance from the river outlets (Figure 5B).

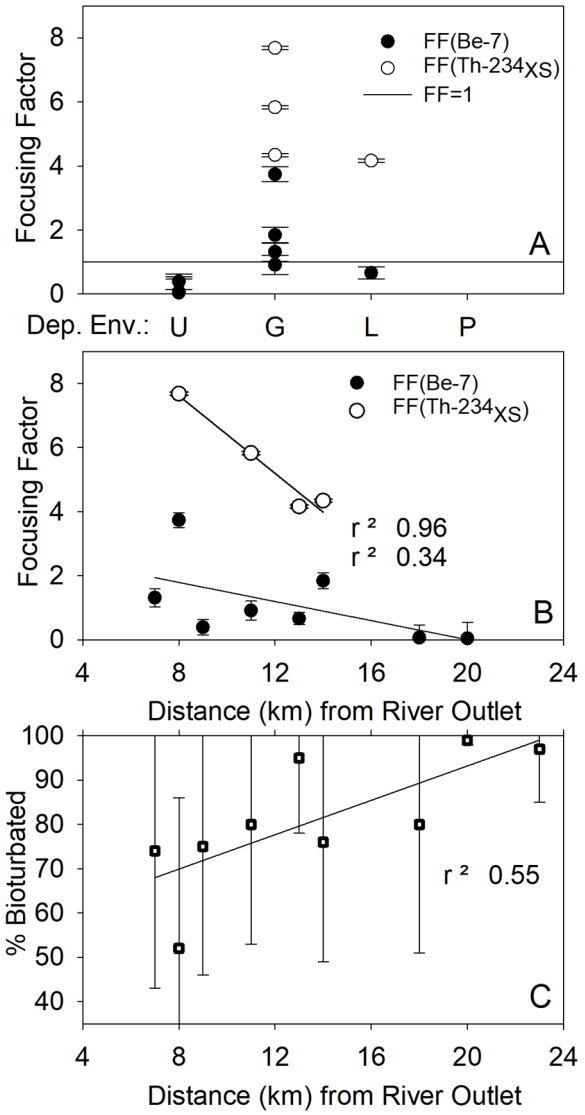

Figure 5. Focusing factors from core inventories of Beryllium-7 and excess Thorium-234 categorized by morphology (undisturbed upper foreset: U, gully: G, lobe: L and prodelta: P) (**A**) and by distance from river outlet (**B**). Focusing factor calculated using Equation (6). Focusing factors > 1 for both Beryllium-7 and excess Thorium-234 are present only at locations with gully morphology. Panel (**C**) shows a summary of mean bioturbation volume percentage ± standard deviation derived from X-radiographs. Panel (**B**) shows that focusing factor decreases with increasing distance from river outlet and panel (**C**) shows that % bioturbation increases with increasing distance from river outlet.

3.2. Grain Size Analysis

Figure 6 shows volume–frequency data for the cores located off of SW Pass (PS17-01, 02, 03 and 05) and deeper water off of S Pass (PS17-32 and 42). On average, the cores

contain ~25% clay, ~69% silt and ~6% sand, with a modal grain size of very fine to fine silt. The SW Pass cores tend to show greater downcore variations in modal grain size (evident in the lateral variations of the warmest colors) than do the cores from the deeper water off of S Pass. The clay and sand content in cores ranges from ~20 to 32% and ~2 to 11%, respectively. The highest clay content occurs off of S Pass (PS17-32), which is the deepest site (258 m) throughout the study area, containing ~32% clay. The SW Pass core locations in shallow water proximal to the MR's main distributaries coincide with the cores containing the greatest sand content, ranging from ~7 to 11%.

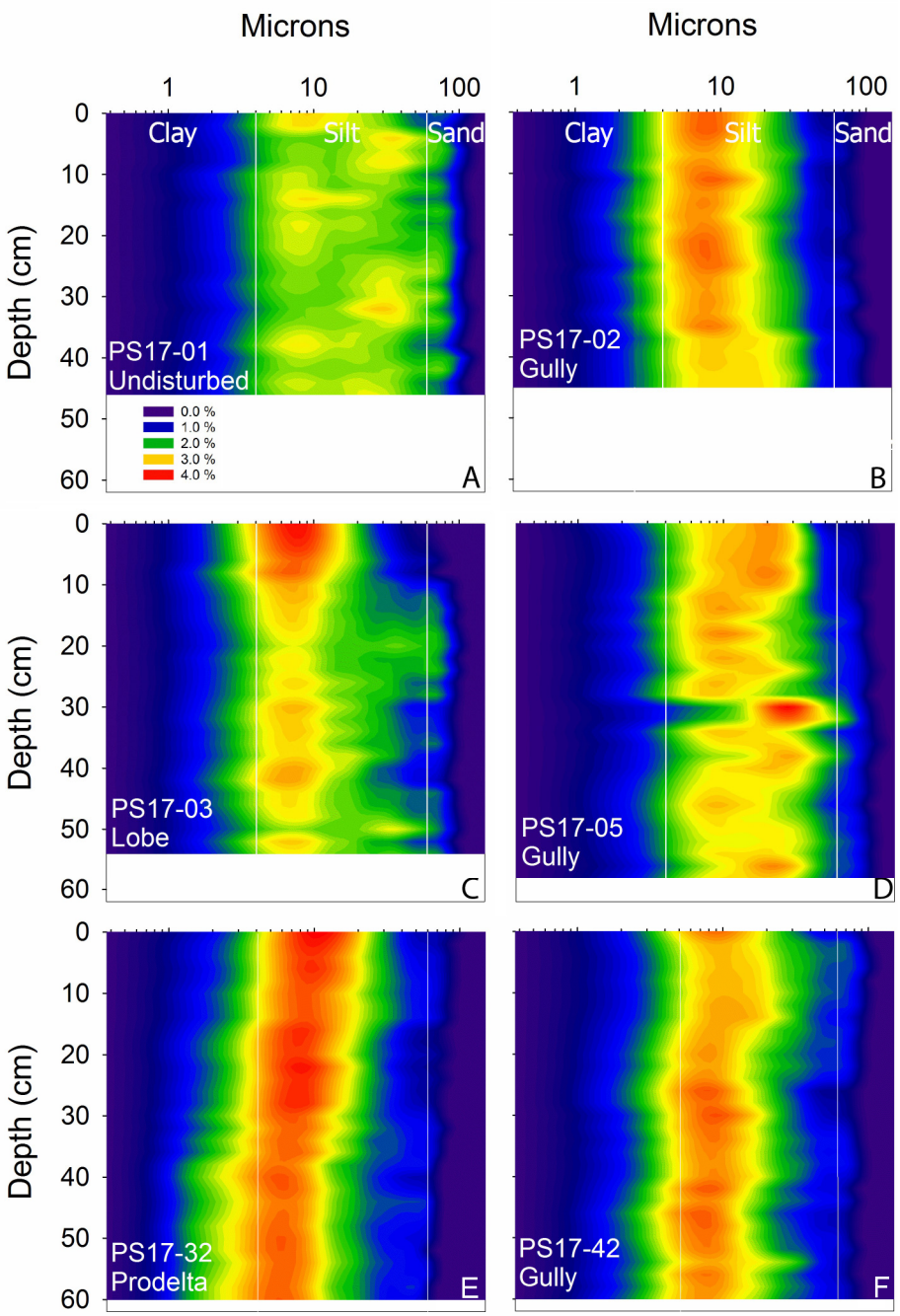

Figure 6. Grain size analysis reported as volume–frequency for cores located off of Southwest Pass (**A**–**D**) and South Pass (**E**,**F**). Clay, silt and sand size class boundaries are denoted along with seafloor morphologies. Silt is the predominant size class observed across all morphologies (**A**–**F**).

3.3. X-Radiography

The X-radiographic images for two SW Pass cores (PS17-03 and 05) and PAL (PS7-91) are shown in Figure 7, including annotations for selected physical and biogenic sedimentary structures, as well as ^{7}Be and $^{234}Th_{xs}$ penetration depths. The three cores imaged in Figure 7 are each located in relatively shallow water (27–60 m) and close to river outlets (8–14 km). They show a mixture of prominent physical stratification (PS17-05 and 91), prominent burrows (annotated in PS-17-05) and faintly mottled fabric (much of PS-17-03). Figure 5C shows an overall increase in the average volume % bioturbation per core with increasing distance from the river outlet. A crossplot of the % bioturbation versus depositional environment (i.e., similar to Figure 5A) showed no obvious trends.

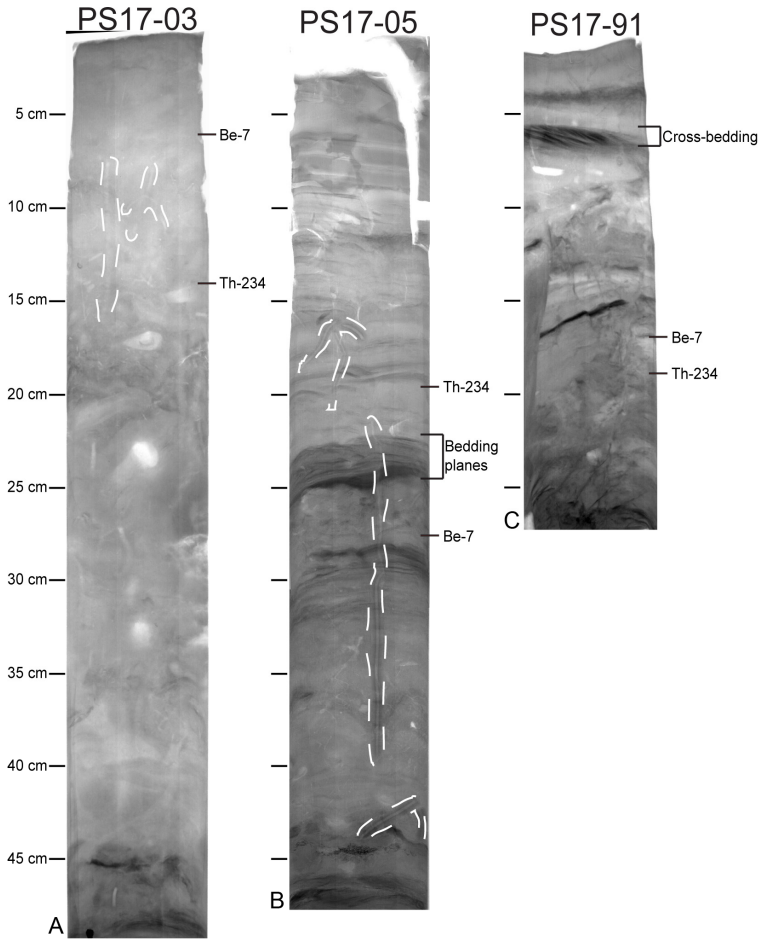

Figure 7. X-radiographs and sedimentary features denoted for cores located off of Southwest Pass ((**A**) lobes and (**B**) gullies) and Pass a Loutre ((**C**) gullies). Lowest detection depths for Beryllium-7 and excess Thorium-234 are shown. Examples of observed sedimentary features include bioturbation (white dashed lines), bedding planes (section denoted in black) and cross-bedding (section denoted in black). Scale bars are shown to the left of X-radiograph images at 5 cm intervals.

3.4. Bed Shear Stress Analysis

The wave-generated bed shear stress for a three-month period around the time of the core collection is shown for water depths of 30 m and 60 m in Figure 8. Modeling and laboratory studies for resuspending the freshly deposited sediment from Mississippi River plumes with critical shear stresses of 0.1–0.3 Pa are required for resuspension [51,52]. Figure 8 indicates that resuspension likely occurred at the 60 m water depth at least once during the observed period during the passage of Tropical Storm Cindy, and resuspension likely occurred at least four times during the same period at water depths of 30 m. Wave-supported resuspension likely is less frequent at water depths >60 m, suggesting that

sediment resuspension assisted by waves occurs at least annually for six out of the nine coring locations studied here.

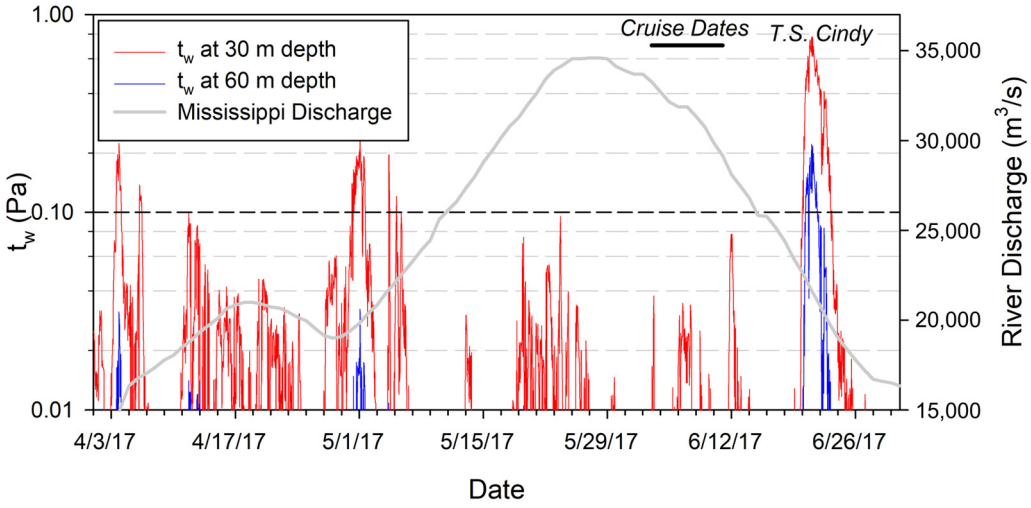

Figure 8. Bed shear stresses at varying depths (30 m—red line and 60 m—blue line) estimated [49,50] from wave data of NOAA buoy 42040 (https://www.ndbc.noaa.gov/, accessed on 7 December 2022), for the time around 2017 coring activities. Buoy 42040 is in deeper water ~110 km SW of the MRDF, so wave height for MRDF water depths was estimated [49]. MR discharge data from USGS 07295100 (https://waterdata.usgs.gov/nwis/sw, accessed on 7 December 2022), Tarbert Landing, MS (gray line), timing of Tropical Storm Cindy (T.S. Cindy), dates of field collection (cruise dates) and approximate resuspension threshold for coarse silt (dashed black line) are denoted.

4. Discussion

Sediment discharge via the MR is the primary sediment source to the MRDF, and recent studies have shown that sediment deposition is concentrated within ~30 km of the river's main distributaries [24], mostly attributed to sedimentation from the river plume. Keller et al. (2017) [18] identified a broad ^{7}Be-laden blanket of sediment thinning offshore from SW Pass, with no obvious trend associated with depositional environments, such as gullies, lobes or prodeltas, consistent with Corbett et al. (2004) [24] and Xu et al. (2011) [53]. It also showed no obvious patterns consistent with gravity-driven remobilization into gullies or otherwise downslope. After the initial deposition, waves, tides, currents and sediment gravity flows can all redistribute sediment in multiple stages through fluvial–marine dispersal systems [8,28].

The downslope flow of sediment into gullies and thence onto lobes is a prime example of such multi-stage sediment dispersal in the MRDF. This can likely occur either as purely gravity-driven flow or alternatively as hydrodynamic resuspension (waves and currents), transport in the water column and redeposition in a time and place under a lower bed shear stress [8,28]. Because gullies are generally deeper than the surrounding seabed (e.g., Figure 2), and because wave-generated shear stresses for specific wave conditions decline with increasing depth, gullies may be more prone to sediment deposition and trapping than the adjacent, more exposed and elevated seabed (Figure 8). The results in Figure 8 indicate that sediment resuspension by waves alone at ~30–60 m depths is routine in the study area, albeit less frequent in deeper water.

The grain size analysis from the core locations off of SW Pass (PS17-01, PS17-02 and PS17-03) may reflect the transport of sediment downslope. The core sites are located in a transect from shallow to deep water (PS17-01 at 31 m, PS17-02 at 51 m and PS17-03 at 60 m). The grain size analysis of the cores shows that PS17-01 has the highest percentage of sand, followed by PS17-03 and PS17-02. It can be expected that locations proximal to the river contain coarser grain sizes due to settling velocities decreasing as the MR enters the Gulf of Mexico. The low occurrence of sand at PS17-02 and the appearance of sand in two

intervals of PS17-03 may suggest the transport of material downslope from the mudflow gullies to lobes.

A radionuclide analysis of the short-lived isotope ^{7}Be serves as a useful tracer of newly deposited material sourced from the MR and in determining short-term sediment deposition rates [18,24,25]. Due to its short half-life ($t_{1/2}$ = 53.2 days), it is assumed that a major source of ^{7}Be is sediment deposition from the MR prior to field collection (June 2017), which captures the sedimentation of the previous ~six to eight months. Figure 8 displays a hydrograph of the MR discharge from Tarbert Landing station, indicating that the high discharge precedes the core collection by 10–15 days (Figure 8). Areas of high sediment accumulation along the MRDF in this study correspond with the MR's dominant distributaries of sediment transport. SW Pass remains the dominant distributary of the MR, transporting most of the sediment load and exhibiting the highest SDR throughout the MRDF [34]. The inventories of the cores analyzed for the excess ^{234}Th inventory were greater than the calculated theoretical inventory, indicating that sediment focusing was taking place at these locations. The SDRs calculated from the excess ^{234}Th were approximately double the SDRs derived from the ^{7}Be data at three core locations (PS17-02, PS17-03 and PS17-91). Time-dependent variations in SDRs have been observed elsewhere [54]; this difference could possibly result from the shorter half-life of ^{234}Th (compared to that of ^{7}Be), allowing ^{234}Th profiles to record sedimentation processes varying over shorter timescales (~3 months) than is possible with the longer-lived ^{7}Be (~6–8 months). Generally, the ^{7}Be inventories and penetration depths were highest throughout the SW Pass study site (Table 2). PAL ranked the second highest in the ^{7}Be inventory, followed by S Pass. The greatest ^{7}Be inventories and activities were observed within 30 km of the MR, coinciding with previous findings [18,24]. Localized rapid sedimentation across the MRDF is known to precondition the seafloor for submarine landslide events [23]. Accordingly, short-term ^{7}Be SDRs can provide insight into what areas along the MRDF may be more prone to mass wasting events occurring on longer timescales (annual to decadal). Based on the fact that rapid sedimentation contributes to mass wasting events and that the highest ^{7}Be SDRs observed were off of SW Pass, this area may be more preconditioned to mass failures at present than S Pass and PAL.

From the seafloor morphological facies sampled (the undisturbed upper foresets, mudflow gully, mudflow lobe and prodelta), the mudflow gullies throughout the MRDF recorded the highest SDRs, inventories and penetration depths derived from the ^{7}Be data (Table 2). It is important to note that only one SDR from an undisturbed seafloor location was suitable for our regression analysis (PS17-01). Two other undisturbed seafloor core sites (PS17-20 and PS17-26), located approximately 18–20 km from the nearest river outlet, only exhibited ^{7}Be activity to a depth of 2 cm, which was insufficient for our regression analysis. However, despite the lack of regression results for SDRs in these cores, the shallow penetration depth of ^{7}Be at these locations is also suggestive of relatively slow sedimentation. The values of R^2 for ^{7}Be SDRs range from 0.08 to 0.97 (Table 2); Equation (1) used for these regressions is a solution for steady-state sedimentation over the timescale of observation. As a result, observations of low R^2 in the cores containing substantial ^{7}Be (e.g., Figure 4C) can be attributed to some interruption of the steady processes that can mix sediments, such as through bioturbation, physical resuspension or mass deposition [24]. The lowest SDR R^2 correlation calculated for ^{7}Be (0.08) was at site PS17-05. The X-radiography (Figure 7) at this site reveals low bioturbation with the sedimentary fabric primarily intact, leading to mass deposits as the cause of the low correlation.

The evidence for sediment focusing was assessed using the approaches described above for Equations (2)–(6). For comparison, two studies, with field locations similar in latitude to the MRDF, were used for a theoretical ^{7}Be inventory. Two mudflow gully locations (PS17-05, SW Pass; and PS17-91, PAL), exhibited higher ^{7}Be inventories than the inventory calculated by Baskaran et al. (1993) [46] for atmospheric deposition only. Three additional sites (PS17-02 and PS17-03, SW Pass; and PS17-42, S Pass) exhibited higher ^{7}Be inventories than the inventory used by Corbett et al. (2004) [24]. These findings indicate

that seafloor morphologies of mudflow gullies and mudflow lobes experience sediment focusing. Possible scenarios for sediment focusing at mudflow gullies and lobes include the following:

(1) Gullies and lobes receive more sediment because gravity flows develop during sediment deposition;
(2) Wave-enhanced sediment gravity flows (WESGFs) occur with the resuspension of river-borne sediment [6];
(3) The resuspension of sediment from undisturbed seafloor and ridges occurs due to higher bed shear stresses from waves, followed by preferential sediment deposition in gullies and deeper water sites with lower bed shear stresses.

To assess the effects of distance from the river outlet on the sediment deposition, SW Pass core sites PS17-01 (uuf), PS17-02 (gul) and PS17-03 (lob) were arranged in an inshore–offshore transect (Figure 2). The ^{7}Be core inventory, ^{7}Be penetration depth and SDR for site PS17-01, located on undisturbed seafloor and proximal to SW Pass, are all lower than the measurements recorded at sites PS17-02 and PS17-03, which are located farther offshore and in deeper water. In addition, site PS17-05 (gul) off of SW Pass is located at a similar water depth and distance from the river-mouth as site PS17-01, but registers a substantially higher ^{7}Be inventory, SDR and penetration depth. ^{7}Be inventories from cores located off of SW Pass exhibit greater inventories than the theoretical inventory used by Corbett et al. (2004) [24], with the exception of PS17-01. Cores PS17-42 off of S Pass and PS17-91 off of PAL are located at similar water depths (±1 m) and have similar morphologies (mudflow gullies) but different distances from the river-mouth (PS17-42, 7 km; and PS17-91, 14 km). Also, recent research has shown that the two distributaries, S Pass and PAL, have similar sediment discharges [34].

These similarities between sites, with the primary difference being the distance from the river-mouth, provide sufficient information to evaluate the possible controls on sediment focusing. It was found that both sites experience sediment focusing when compared to the theoretical inventory used by Corbett et al. (2004) [24]. However, PS17-91 (PAL) located 7 km farther offshore than PS17-42 (S Pass), exhibits a higher ^{7}Be inventory and SDR than those of PS17-42. The ^{7}Be data from the SW Pass cores and core sites located in the gullies off S Pass and PAL indicate that other mechanisms, besides their proximity to the river-mouth, primarily control the sediment focusing of ^{7}Be-laden sediment at locations with known morphologies of mudflow gullies and lobes. It is important to note that all of the ^{7}Be core inventories calculated from undisturbed seafloor locations had lower inventories than both the theoretical inventories used from Baskaran et al. (1993) [46] and Corbett et al. (2004) [24]. These findings indicate that sediment focusing is correlated with the specific seafloor morphologies of mudflow gullies and mudflow lobes and that these morphologies are primary locations of sediment deposition along the MRDF.

Wave and/or current influence on the seafloor is evident in X-radiographic images of PS17-91, off of PAL, where cross-bedding is present (Figure 7). The X-radiograph images throughout the rest of the study area only exhibit planar bedding features, potentially indicating vertical deposition from sediment plumes. The findings of excess ^{234}Th inventories greater than the calculated ^{234}Th theoretical inventory combined with the presence of cross-bedding suggest that waves and/or currents have a strong influence across the MRDF, specifically at core site PS17-91. It is noted that currents play an important role in the transportation of sediment. However, river flow and waves are the main influences on the deposition and resuspension of fluvial and marine sediments on the Louisiana shelf [25]. The X-radiography of core sites throughout the study region show a general trend of increasing bioturbation as the water depth and distance from the MR increase.

Core sites proximal to the river-mouth experience high SDRs, an increased presence of bedding and low bioturbation in comparison to core sites located farther offshore, which exhibit high rates of bioturbation. The bioturbation plots and X-radiograph images of the cores taken off of SW Pass and S Pass display this relationship. This is directly related to the preservation potential of sedimentary event layers [29,55]. The physical stratification

in the cores proximal to the MR have a higher preservation potential compared to distal sites, a pattern that has been well established for the MR [56]. The X-radiograph images indicate that the biogenic sedimentary fabric is likely to overprint the sedimentary fabric when the rate of bioturbation greatly exceeds the net combined rates of physical reworking and deposition [29].

5. Conclusions

This research provides a regional survey of active sediment deposition offshore of major MR outlets using short-lived radioisotopes, contributing to our understanding of sedimentary processes that influence sediment mass transport. Historic changes to the sediment load of the MR and sediment dispersal patterns along the MRDF have strong influences on submarine landslides temporally and spatially, highlighting the significance of this study. The major conclusions of this study are as follows:

(1) Despite substantial reductions in the MR sediment load, our ^{7}Be analysis shows the active sediment deposition of fluvially sourced sediment offshore from all three major outlets;
(2) Our ^{7}Be analysis shows that the core sites proximal to the river-mouth received the greatest amount of sediment and decreased offshore. SW Pass experienced the highest sediment deposition rates (0.2 cm/day on average), followed by PAL and S Pass;
(3) The mudflow gully locations exhibit the highest sediment deposition rates, derived from our ^{7}Be analysis, out of all of the environments studied (undisturbed upper foresets, mudflow gully, mudflow lobe and prodelta) across the entire sampling area;
(4) Sediment focusing was determined at five core locations (one lobe and two gully sites off of SW Pass; one gully site off of S Pass; and one gully site off of PAL) based on theoretical ^{7}Be inventories used by Corbett et al. (2004) [24];
(5) The sediment deposition rates determined from the excess ^{234}Th for sites PS17-02, PS17-03 and PS17-91 were double those determined from ^{7}Be, suggesting a strong influence from waves and/or currents on the redistribution of sediment;
(6) The X-radiograph analysis of the cores shows a general trend of increasing bioturbation present as the distance offshore increases, with core sites proximal to the river-mouth more likely to preserve bedding layers.

Based on the direct relationship between the sediment load of the MR and sediment deposition on the delta front, future surveys should be considered in light of coastal restoration efforts using the MR for proposed sediment diversions [57]. The construction of the proposed sediment diversions will result in a loss of sediment arriving at the MRDF and will likely lead to delta front degradation and affect the timing and occurrence of mass wasting events.

Supplementary Materials: The following supporting can be downloaded at: Courtois, Andrew J., "A Regional Survey of River-plume Sedimentation on the Mississippi River Delta Front" (2018). LSU Master's Theses. 4807. https://digitalcommons.lsu.edu/gradschool_theses/4807. Accessed on 15 November 2023 [41].

Author Contributions: Writing—original draft preparation, A.C. and S.B.; writing—review and editing, A.C., S.B., J.M., K.X., J.C., I.Y.G., M.D.M., J.O., N.H.J., M.D.; data curation, A.C., S.B., J.C.; conceptualization, S.B., A.C.; investigation, A.C., S.B., J.M., J.C., I.Y.G., J.O., N.H.J.; funding acquisition, S.B. All authors have read and agreed to the published version of the manuscript.

Funding: Funding for this study was provided by the U.S. Department of the Interior, Bureau of Ocean Energy Management, Coastal Marine Institute, Washington DC, under Cooperative Agreement Number M13AC00013. Additional support was provided from the Billy and Ann Harrison Endowment in Sedimentary Geology, Louisiana State University Department of Geology and Geophysics.

Data Availability Statement: The river discharge and wave data used in this study can be obtained from the United States Geological Survey (https://waterdata.usgs.gov/nwis/sw), accessed 7 December 2022, and National Atmospheric and Oceanic Administration (https://www.ndbc.noaa.gov/)

accessed 7 December 2022, respectively. The bathymetric and seismic data can be obtained from the United States Geological Survey [26]. The field measurement data during this study and the analysis data are available from the corresponding author upon reasonable request.

Acknowledgments: The authors would like to sincerely thank the Louisiana State University Coastal Studies Institute for its technical support in the lab and in our fieldwork, as well as Kanchan Maiti of Louisiana State University for supplying the CTD data. Any use of trade, firm, or product names is for descriptive purposes only and does not imply endorsement by the U.S. Government.

Conflicts of Interest: The authors declare no conflicts of interest.

References

1. Hampton, M.A.; Lee, H.J.; Locat, J. Submarine Landslides. *Rev. Geophys.* **1996**, *34*, 33–59. [CrossRef]
2. Maloney, J.M.; Bentley, S.J.; Xu, K.; Obelcz, J.; Georgiou, I.Y.; Jafari, N.H.; Miner, M.D. Mass Wasting on the Mississippi River Subaqueous Delta. *Earth-Sci. Rev.* **2020**, *200*, 103001. [CrossRef]
3. Henkel, D. The Role of Waves in Causing Submarine Landslides. *Geotechnique* **1970**, *20*, 75–80. [CrossRef]
4. Wright, L.; Friedrichs, C.; Kim, S.; Scully, M. Effects of Ambient Currents and Waves on Gravity-Driven Sediment Transport on Continental Shelves. *Mar. Geol.* **2001**, *175*, 25–45. [CrossRef]
5. Walsh, J.; Nittrouer, C. Understanding Fine-Grained River-Sediment Dispersal on Continental Margins. *Mar. Geol.* **2009**, *263*, 34–45. [CrossRef]
6. Macquaker, J.H.S.; Bentley, S.J.; Bohacs, K.M. Wave-Enhanced Sediment-Gravity Flows and Mud Dispersal across Continental Shelves: Reappraising Sediment Transport Processes Operating in Ancient Mudstone Successions. *Geology* **2010**, *38*, 947–950. [CrossRef]
7. Falcini, F.; Fagherazzi, S.; Jerolmack, D. Wave-Supported Sediment Gravity Flows Currents: Effects of Fluid-Induced Pressure Gradients and Flow Width Spreading. *Cont. Shelf Res.* **2012**, *33*, 37–50. [CrossRef]
8. Puig, P.; Ogston, A.S.; Mullenbach, B.; Nittrouer, C.; Parsons, J.; Sternberg, R. Storm-induced Sediment Gravity Flows at the Head of the Eel Submarine Canyon, Northern California Margin. *J. Geophys. Res. Oceans* **2004**, *109*. [CrossRef]
9. Coleman, J.M.; Prior, D.B. Subaqueous Sediment Instabilities in the Offshore Mississippi River Delta: Section 5. In *CN 18: Offshore Geologic Hazards*; Bureau of Land Management: New Orleans, LA, USA, 1981; Volume 87, pp. 1–53.
10. Day, J.W.; Kemp, G.P.; Freeman, A.M.; Muth, D.P. *Perspectives on the Restoration of the Mississippi Delta: The Once and Future Delta*; Springer: Berlin/Heidelberg, Germany, 2014; ISBN 978-94-017-8733-8.
11. Coleman, J.M.; Suhayda, J.N.; Whelan, T.; Wright, L.D. Mass Movement of Mississippi River Delta Sediments. *Gulf Coast Assoc. Geol. Soc. Trans.* **1974**, *24*, 49–68.
12. Prior, D.B.; Suhayda, J.N. Submarine Mudslide Morphology and Development Mechanisms, Mississippi Delta. In Proceedings of the Offshore Technology Conference, OnePetro, Houston, TX, USA, 30 April 1979.
13. Coleman, J.M.; Prior, D.B. (Eds.) Characteristics of Deltaic Depositional Environments. In *Deltaic Sand Bodies*; American Association of Petroleum Geologists: Tulsa, OK, USA, 1980; Volume 15, ISBN 978-1-62981-182-6.
14. Obelcz, J.; Xu, K.; Georgiou, I.Y.; Maloney, J.; Bentley, S.J.; Miner, M.D. Sub-Decadal Submarine Landslides Are Important Drivers of Deltaic Sediment Flux: Insights from the Mississippi River Delta Front. *Geology* **2017**, *45*, 703–706. [CrossRef]
15. Maloney, J.M.; Bentley, S.J.; Xu, K.; Obelcz, J.; Georgiou, I.Y.; Miner, M.D. Mississippi River Subaqueous Delta Is Entering a Stage of Retrogradation. *Mar. Geol.* **2018**, *400*, 12–23. [CrossRef]
16. Blum, M.D.; Roberts, H.H. Drowning of the Mississippi Delta Due to Insufficient Sediment Supply and Global Sea-Level Rise. *Nat. Geosci.* **2009**, *2*, 488–491. [CrossRef]
17. Chaytor, J.D.; Baldwin, W.E.; Bentley, S.J.; Damour, M.; Jones, D.; Maloney, J.; Miner, M.D.; Obelcz, J.; Xu, K. Short- and Long-Term Movement of Mudflows of the Mississippi River Delta Front and Their Known and Potential Impacts on Oil and Gas Infrastructure. *Geol. Soc. Lond. Spec. Publ.* **2020**, *500*, 587–604. [CrossRef]
18. Keller, G.; Bentley, S.J.; Georgiou, I.Y.; Maloney, J.; Miner, M.D.; Xu, K. River-Plume Sedimentation and 210Pb/7Be Seabed Delivery on the Mississippi River Delta Front. *Geo-Mar. Lett.* **2017**, *37*, 259–272. [CrossRef]
19. BOEM Offshore Analysis of Seafloor Instability and Sediments (OASIS Partnership) with Applications to Offshore Safety and Marine Archaeology (GM-21-01). Available online: https://www.boem.gov/environment/gm-21-01 (accessed on 3 December 2023).
20. Sterling, G.H.; Strohbeck, E. The Failure of the South Pass 70 "B" Platform Hurricane Camille. In Proceedings of the 5th Offshore Technology Conference OTC, Houston, TX, USA, 29 April–2 May 1973; p. OTC-1898.
21. Bea, R.G. How Sea-Floor Slides Affect Offshore Structures. *Oil Gas J.* **1971**, *69*, 88–93.
22. Murawski, S.A.; Hollander, D.J.; Gilbert, S.; Gracia, A. Deepwater Oil and Gas Production in the Gulf of Mexico and Related Global Trends. In *Scenarios and Responses to Future Deep Oil Spills: Fighting the Next War*; Murawski, S.A., Ainsworth, C.H., Gilbert, S., Hollander, D.J., Paris, C.B., Schlüter, M., Wetzel, D.L., Eds.; Springer International Publishing: Cham, Switzerland, 2020; pp. 16–32, ISBN 978-3-030-12963-7.
23. Coleman, J.M. Dynamic Changes and Processes in the Mississippi River Delta. *GSA Bull.* **1988**, *100*, 999–1015. [CrossRef]

24. Corbett, D.R.; McKee, B.; Duncan, D. An Evaluation of Mobile Mud Dynamics in the Mississippi River Deltaic Region. *Mar. Geol.* **2004**, *209*, 91–112. [CrossRef]
25. Corbett, D.R.; Dail, M.; McKee, B. High-Frequency Time-Series of the Dynamic Sedimentation Processes on the Western Shelf of the Mississippi River Delta. *Cont. Shelf Res.* **2007**, *27*, 1600–1615. [CrossRef]
26. Baldwin, W.E.; Ackerman, S.D.; Worley, C.R.; Danforth, W.W.; Chaytor, J.D. High-Resolution Geophysical Data Collected along the Mississippi River Delta Front Offshore of Southeastern Louisiana, U.S. Geological Survey Field Activity 2017-003-FA: U.S. Geological Survey Data Release, 2018. Available online: https://www.sciencebase.gov/catalog/item/5a8c4bcbe4b00f54eb44044c (accessed on 3 December 2023).
27. Wright, L.; Nittrouer, C. Dispersal of River Sediments in Coastal Seas: Six Contrasting Cases. *Estuaries* **1995**, *18*, 494–508. [CrossRef]
28. Puig, P.; Ogston, A.; Mullenbach, B.; Nittrouer, C.; Sternberg, R. Shelf-to-Canyon Sediment-Transport Processes on the Eel Continental Margin (Northern California). *Mar. Geol.* **2003**, *193*, 129–149. [CrossRef]
29. Bentley, S.J.; Sheremet, A.; Jaeger, J.M. Event Sedimentation, Bioturbation, and Preserved Sedimentary Fabric: Field and Model Comparisons in Three Contrasting Marine Settings. *Cont. Shelf Res.* **2006**, *26*, 2108–2124. [CrossRef]
30. Hitchcock, C.; Givler, R.; Angell, M.; Hooper, J. GIS-Based Assessment of Submarine Mudflow Hazard Offshore of the Mississippi Delta, Gulf of Mexico. In *Submarine Mass Movements and Their Consequences*; Mosher, D.C., Shipp, R.C., Moscardelli, L., Chaytor, J.D., Baxter, C.D.P., Lee, H.J., Urgeles, R., Eds.; Advances in Natural and Technological Hazards Research; Springer: Dordrecht, The Netherlands, 2010; pp. 353–364, ISBN 978-90-481-3071-9.
31. Galloway, W.E. *Process Framework for Describing the Morphologic and Stratigraphic Evolution of Deltaic Depositional Systems*; Houston Geological Society: Houston, TX, USA, 1975; pp. 87–98.
32. Blum, M.; Rahn, D.; Frederick, B.; Polanco, S. Land Loss in the Mississippi River Delta: Role of Subsidence, Global Sea-Level Rise, and Coupled Atmospheric and Oceanographic Processes. *Glob. Planet. Chang.* **2023**, *222*, 104048. [CrossRef]
33. Meade, R.H.; Moody, J.A. Causes for the Decline of Suspended-sediment Discharge in the Mississippi River System, 1940–2007. *Hydrol. Process. Int. J.* **2010**, *24*, 35–49. [CrossRef]
34. Allison, M.A.; Demas, C.R.; Ebersole, B.A.; Kleiss, B.A.; Little, C.D.; Meselhe, E.A.; Powell, N.J.; Pratt, T.C.; Vosburg, B.M. A Water and Sediment Budget for the Lower Mississippi–Atchafalaya River in Flood Years 2008–2010: Implications for Sediment Discharge to the Oceans and Coastal Restoration in Louisiana. *J. Hydrol.* **2012**, *432–433*, 84–97. [CrossRef]
35. Milliman, J.D.; Meade, R.H. World-Wide Delivery of River Sediment to the Oceans. *J. Geol.* **1983**, *91*, 1–21. [CrossRef]
36. Usace Beneficial Use of Dredged Material Disposal History Mississippi River, Baton Rouge to the Gulf of Mexico, LA Head of Passes Hopper Dredge Disposal Area. Available online: https://www.mvn.usace.army.mil/Portals/56/HDDA%20BU%20History%202015-2020.pdf (accessed on 3 December 2023).
37. Allison, M.A.; Meselhe, E.A.; Kleiss, B.A.; Duffy, S.M. Impact of Water Loss on Sustainability of the Mississippi River Channel in Its Deltaic Reach. *Hydrol. Process.* **2023**, *37*, e15004. [CrossRef]
38. Coleman, J.M.; Roberts, H.H.; Stone, G.W. Mississippi River Delta: An Overview. *J. Coast Res.* **1998**, *14*, 698–716.
39. Patruno, S.; Helland-Hansen, W. Clinoforms and Clinoform Systems: Review and Dynamic Classification Scheme for Shorelines, Subaqueous Deltas, Shelf Edges and Continental Margins. *Earth-Sci. Rev.* **2018**, *185*, 202–233. [CrossRef]
40. Nodine, M.C.; Cheon, J.Y.; Wright, S.G.; Gilbert, R.B. *Mudslides during Hurricane Ivan and an Assessment of the Potential for Future Mudslides in the Gulf of Mexico*; MMS Project Number 552; Offshore Technology Research Center: Austin, TX, USA, 2007.
41. Courtois, A.J. A Regional Survey of River-Plume Sedimentation on the Mississippi River Delta Front. Master's Thesis, Louisiana State University and Agricultural and Mechanical College, Baton Rouge, LA, USA, 2018.
42. Olsen, C.; Larsen, I.; Lowry, P.; Cutshall, N.; Nichols, M. Geochemistry and Deposition of 7Be in River-estuarine and Coastal Waters. *J. Geophys. Res. Oceans* **1986**, *91*, 896–908. [CrossRef]
43. Young, D.R. *Examination of the 2011 Mississippi River Flood Deposit on the Louisiana Continental Shelf*; East Carolina University: Greenville, NC, USA, 2014; ISBN 1-321-18924-9.
44. Cochran, J.K.; Masqué, P. Short-Lived U/Th Series Radionuclides in the Ocean: Tracers for Scavenging Rates, Export Fluxes and Particle Dynamics. *Rev. Mineral. Geochem.* **2003**, *52*, 461–492. [CrossRef]
45. Muhammad, Z.; Bentley, S.J.; Febo, L.A.; Droxler, A.W.; Dickens, G.R.; Peterson, L.C.; Opdyke, B.N. Excess 210Pb Inventories and Fluxes along the Continental Slope and Basins of the Gulf of Papua. *J. Geophys. Res. Earth Surf.* **2008**, *113*. [CrossRef]
46. Baskaran, M.; Coleman, C.H.; Santschi, P.H. Atmospheric Depositional Fluxes of 7Be and 210Pb at Galveston and College Station, Texas. *J. Geophys. Res. Atmos.* **1993**, *98*, 20555–20571. [CrossRef]
47. Owens, S.; Buesseler, K.; Sims, K. Re-Evaluating the 238U-Salinity Relationship in Seawater: Implications for the 238U–234Th Disequilibrium Method. *Mar. Chem.* **2011**, *127*, 31–39. [CrossRef]
48. Adhikari, P.L.; Maiti, K.; Overton, E.B.; Rosenheim, B.E.; Marx, B.D. Distributions and Accumulation Rates of Polycyclic Aromatic Hydrocarbons in the Northern Gulf of Mexico Sediments. *Environ. Pollut.* **2016**, *212*, 413–423. [CrossRef] [PubMed]
49. Lo, E.L.; Bentley, S.J.; Xu, K. Experimental Study of Cohesive Sediment Consolidation and Resuspension Identifies Approaches for Coastal Restoration: Lake Lery, Louisiana. *Geo-Mar. Lett.* **2014**, *34*, 499–509. [CrossRef]
50. Xu, K.; Corbett, D.R.; Walsh, J.P.; Young, D.; Briggs, K.B.; Cartwright, G.M.; Friedrichs, C.T.; Harris, C.K.; Mickey, R.C.; Mitra, S. Seabed Erodibility Variations on the Louisiana Continental Shelf before and after the 2011 Mississippi River Flood. *Estuar. Coast. Shelf Sci.* **2014**, *149*, 283–293. [CrossRef]

51. Soulsby, R. *Dynamics of Marine Sands*; Thomas Telford: Telford, UK, 1997.
52. Wright, L.D. *Morphodynamics of Inner Continental Shelves*; CRC Press: Boca Raton, FL, USA, 1995.
53. Xu, K.; Harris, C.K.; Hetland, R.D.; Kaihatu, J.M. Dispersal of Mississippi and Atchafalaya Sediment on the Texas–Louisiana Shelf: Model Estimates for the Year 1993. *Cont. Shelf Res.* **2011**, *31*, 1558–1575. [CrossRef]
54. Sadler, P.M. Sediment Accumulation Rates and the Completeness of Stratigraphic Sections. *J. Geol.* **1981**, *89*, 569–584. [CrossRef]
55. Wheatcroft, R.A. Preservation Potential of Sedimentary Event Layers. *Geology* **1990**, *18*, 843–845. [CrossRef]
56. Moore, D.G.; Scruton, P.C. Minor Internal Structures of Some Recent Unconsolidated Sediments. *AAPG Bull.* **1957**, *41*, 2723–2751. [CrossRef]
57. Coastal Protection and Restoration Authority of Louisiana. *Louisiana's Comprehensive Master Plan for a Sustainable Coast*; Coastal Protection and Restoration Authority of Louisiana: Baton Rouge, LA, USA, 2023.